nature COMMUNICATIONS

ARTICLE

Received 9 Sep 2016 | Accepted 19 Jan 2017 | Published 10 Mar 2017

DOI: 10.1038/ncomms14723 OPEN

A molecule-like $PtAu_{24}(SC_6H_{13})_{18}$ nanocluster as an electrocatalyst for hydrogen production

Kyuju Kwak[1,*], Woojun Choi[1,*], Qing Tang[2], Minseok Kim[1], Yongjin Lee[1], De-en Jiang[2] & Dongil Lee[1]

The theoretically predicted volcano plot for hydrogen production shows the best catalyst as the one that ensures that the hydrogen binding step is thermodynamically neutral. However, the experimental realization of this concept has suffered from the inherent surface heterogeneity of solid catalysts. It is even more challenging for molecular catalysts because of their complex chemical environment. Here, we report that the thermoneutral catalyst can be prepared by simple doping of a platinum atom into a molecule-like gold nanocluster. The catalytic activity of the resulting bimetallic nanocluster, $PtAu_{24}(SC_6H_{13})_{18}$, for the hydrogen production is found to be significantly higher than reported catalysts. It is even better than the benchmarking platinum catalyst. The molecule-like bimetallic nanocluster represents a class of catalysts that bridge homogeneous and heterogeneous catalysis and may provide a platform for the discovery of finely optimized catalysts.

[1] Department of Chemistry, Yonsei University, Seoul 03722, South Korea. [2] Department of Chemistry, University of California, Riverside, California 92521, USA. * These authors contributed equally to this work. Correspondence and requests for materials should be addressed to D.L. (email: dongil@yonsei.ac.kr) or to D.-e.J. (email: de-en.jiang@ucr.edu).

Hydrogen (H_2) has been considered as an alternative energy carrier and generated the intense interest in creating artificial catalytic systems that can efficiently produce H_2 from water[1–4]. Hydrogenase enzymes that contain iron and nickel cofactors are efficient hydrogen evolution reaction (HER) catalysts with turnover frequencies (TOFs) as high as 9,000 mol of H_2 per mole of catalyst per second (mol H_2 (mol cat)$^{-1}$ s^{-1})[5]. There have been a variety of synthetic molecular catalysts, including nickel, cobalt, iron and molybdenum complexes, to mimic the biological catalysts[6–12]. However, the TOF values reported for these complexes remain quite low (<4.1 mol H_2 (mol cat)$^{-1}$ s^{-1}), and they often show limited stability in aqueous media[13]. Moreover, practical electrocatalysis typically requires their immobilization on electrode materials that can operate fully in aqueous media[14,15]. Recent progress in the computational design of solid catalysts has revealed the importance of engineering of the structure and adsorption energies for catalysis at surfaces[16–18]. In fact, some engineered surface alloys exhibit high catalytic activities comparable to platinum[18]. However, the inherent heterogeneity in the surface structure and composition often found in these solid catalysts hamper the fine controlling of these properties at the molecular scale.

Ligand-protected gold and silver nanoclusters have received much attention as materials with many practical applications because of promises offered by their unique optical, electrochemical and catalytic properties[19–22]. Unlike the supported cluster systems[23,24], these clusters are stable without the support and readily soluble in appropriate solvents. They have special stability at certain compositions, and thus molecule-like clusters with precise compositions are typically obtained from various size-controlled syntheses[21,22]. $Au_{25}(SR)_{18}$, $Au_{102}(SR)_{44}$ and $Ag_{44}(SR)_{30}$, where SR is a thiolate ligand, are the examples of these clusters whose stability is thought to arise from the closure of superatomic electron shells[25–27]. While stable clusters to date are rather limited to Au and Ag systems, bimetallic clusters prepared by doping a foreign metal into the stable Au and Ag clusters have opened an avenue to the fine-tuning of the cluster properties[28–33]. Here we report a highly active HER catalyst based on a molecule-like bimetallic cluster that can generate H_2 with TOFs of 4.8 in tetrahydrofuran (THF) and 34 mol H_2 (mol cat)$^{-1}$ s^{-1} in water, respectively, at a moderate overpotential ($\eta = 0.6$ V). This cluster catalyst represents a special type of catalyst that bridges homogeneous and heterogeneous catalysis.

Results

Molecule-like metal nanoclusters. It has been found that Pt can selectively replace the central gold atom in the Au_{25} cluster, leading to a single Pt-doped bimetallic cluster (Fig. 1a)[30,33,34]. The Au_{25} and Pt-doped clusters were synthesized according to the procedures reported elsewhere[34] (see Supplementary Notes 1–3 for details). Although they have been fully characterized in our previous report[34], we will next briefly discuss their mass spectra, and optical and electrochemical properties, which can serve as an introduction to these molecule-like metal clusters. In Fig. 1b, the matrix-assisted laser desorption ionization mass spectra of the isolated gold (red) and Pt-doped gold clusters (blue) show only a single peak, indicating that the isolated clusters are extremely monodisperse. The peak at m/z ~7,034 Da observed for the gold cluster (red) corresponds to the intact ion with a chemical composition of $Au_{25}(SC_6H_{13})_{18}$. The peak at m/z ~7,032 Da observed for the Pt-doped gold cluster is however almost superimposed with that of $Au_{25}(SC_6H_{13})_{18}$ due to their small mass difference. The isotope pattern of the Pt-doped gold cluster (blue) shown in the inset of Fig. 1b can clearly be distinguished from that of $Au_{25}(SC_6H_{13})_{18}$ (red) and matches well with the simulated isotope pattern (black) of $PtAu_{24}(SC_6H_{13})_{18}$, manifesting that one Au atom in the Au_{25} cluster has been cleanly replaced by a Pt atom. Hereafter, these clusters will be abbreviated as Au_{25} and $PtAu_{24}$, respectively. The average core size of both clusters is found to be around 1.1 nm (Supplementary Fig. 1).

The ultraviolet-vis-near-infrared (NIR) absorption spectra in Fig. 1c show distinctively different profiles of Au_{25} and $PtAu_{24}$ clusters. The absorption profile is shown in the photon energy scale to show the broad NIR peak more clearly. The Au_{25} cluster exhibits the characteristic absorption features of Au_{25} clusters with peaks at 1.8, 2.8 and 3.1 eV. On Pt doping, the absorption profile changes drastically; that is, there is a new absorption band that appears at 2.1 eV with an additional NIR band centred at 1.1 eV in the low-energy region. The absorption profile of the Pt-doped cluster is consistent with that of neutral $[PtAu_{24}]^0$ where the Pt dopant is located at the centre of the core[33]. Evidently, replacing the central Au atom with Pt results in stable $[PtAu_{24}]^0$ having a superatomic 6-electron configuration[25,26,34]. The change in superatomic electronic configuration from 8-electron $[Au_{25}]^-$ to 6-electron $[PtAu_{24}]^0$ would lead to the splitting of the 1P orbital accompanying a Jahn–Teller-like distortion of the $PtAu_{12}$ core[34]. The appearance of the new bands at 1.1 eV (α) and 2.1 eV (γ) and the disappearance of the band at 1.8 eV (β) for $[PtAu_{24}]^0$ in Fig. 1c,d are the results of the change in electronic structure of $PtAu_{24}$.

Electrochemistry and electrocatalytic activities. The optical measurements show that the electronic structure of Au_{25} cluster is drastically altered on doping of a Pt atom. To further unravel the electronic structure of the $PtAu_{24}$ cluster, square-wave voltammetry (SWV) of Au_{25} and $PtAu_{24}$ clusters were conducted. Voltammetry has been effectively used to study the electron transfer properties and the electronic structures of gold nanoclusters[19,34]. Understanding the redox behaviours near the HOMO-LUMO (highest occupied and lowest unoccupied molecular orbitals) levels is of particular importance in the design of efficient electrocatalysts. The SWVs in Fig. 2a exhibit well-resolved current peaks that lie at the formal potentials of the cluster charge-state couples. The open-circuit potential was found at -0.49 V for the Au_{25} cluster, indicating that the Au_{25} cluster is in anionic form, that is, $[Au_{25}]^-$. Therefore, the current peaks observed at -0.39 (O1), -0.04 (O2) and 0.69 (O3) correspond to the first, second and third oxidation peaks of the $[Au_{25}]^-$ cluster, while the peak at -2.06 V (R1) corresponds to the first reduction peak. The electrochemical gap determined from the difference between the first oxidation (O1) and reduction (R1) potentials is found to be 1.67 V. The HOMO-LUMO gap for $[Au_{25}]^-$ is determined to be 1.32 V by subtracting the charging energy term (O1–O2) of 0.35 V from the O1–R1 gap.

The redox potentials are drastically altered on doping of a Pt atom in the core as can be seen in Fig. 2a. Unlike the anionic Au_{25} cluster, $PtAu_{24}$ is charge neutral with the open-circuit potential found at -0.49 V. Thus, the current peaks observed at -0.03 (O1) and 0.41 (O2) correspond to the first and second oxidation peaks of the $PtAu_{24}$ cluster, while -0.76 (R1) and -1.10 V (R2) correspond to the first and second reduction peaks. The observed O1–R1 gap and the deduced HOMO-LUMO gaps from the SWV in Fig. 2a are found to be dramatically reduced to 0.73 V and 0.29 V, respectively. This result indicates that the electronic structure has indeed been greatly altered on Pt doping, and, more importantly, reduction potentials of $[PtAu_{24}]^0$ shifted positively by nearly 1 V compared to that of $[Au_{25}]^-$, potentially offering the possibility to lower overpotentials for reductive electrocatalysis.

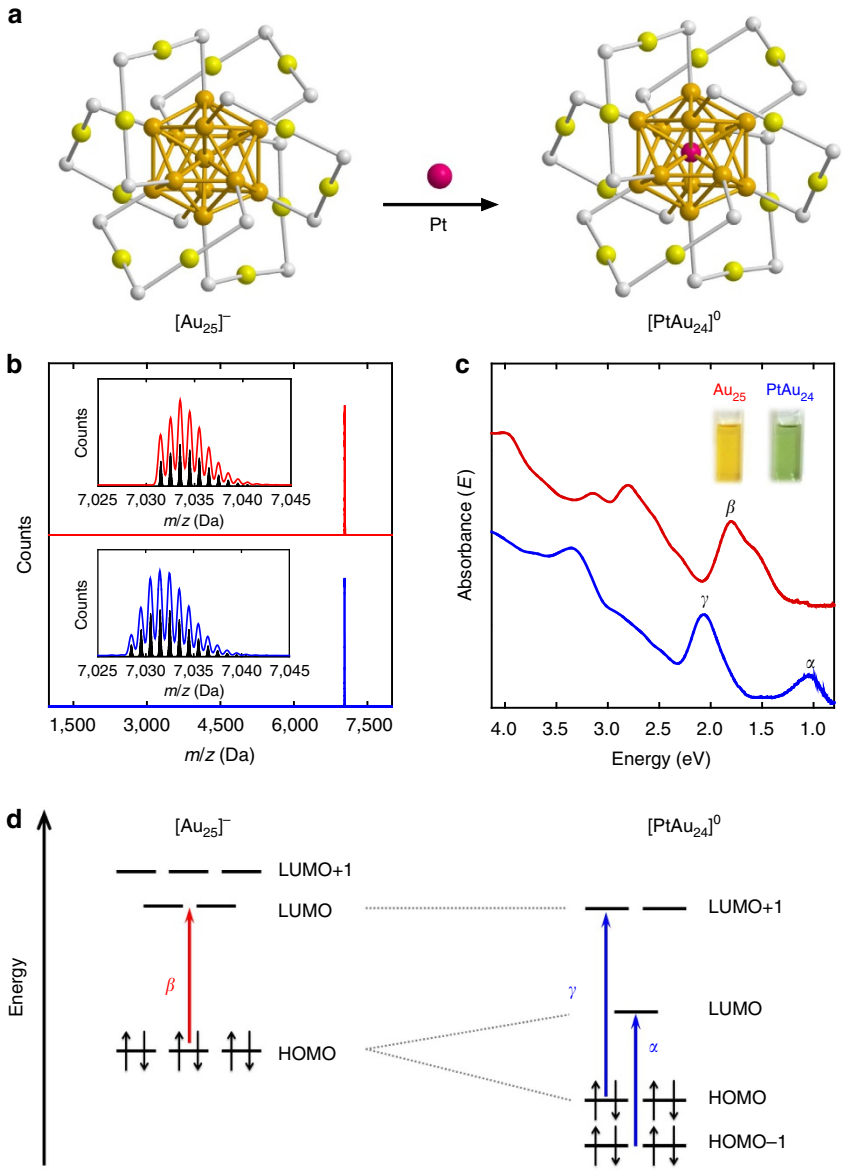

Figure 1 | Characterizations of molecule-like metal clusters. (**a**) Structures of Au_{25} and $PtAu_{24}$ clusters (golden, gold atoms of the core; olive, gold atoms of the shell; grey, sulfur (the rest of the ligand is omitted for clarity)). (**b**) Matrix-assisted laser desorption ionization (MALDI) mass spectra of $Au_{25}(SC_6H_{13})_{18}$ (red) and $PtAu_{24}(SC_6H_{13})_{18}$ (blue). The insets show the comparisons between the experimental data and the simulated isotope patterns (black sticks). (**c**) UV-vis-NIR absorption spectra of $[Au_{25}]^-$ (red) and $[PtAu_{24}]^0$ (blue) in tetrachloroethylene. The wavelength-scale absorption spectrum, Abs(λ), was converted to the energy-scale spectrum, absorbance (E), according to the relation $Abs(E) \propto [Abs(\lambda)]\lambda^2$. The insets show the photographs of $[Au_{25}]^-$ and $[PtAu_{24}]^0$ in CH_2Cl_2. (**d**) Electronic energy levels of $[Au_{25}]^-$ and $[PtAu_{24}]^0$. α, β and γ denote the optical transitions observed for $[Au_{25}]^-$ and $[PtAu_{24}]^0$ in **c**.

Figure 2b shows linear sweep voltammograms (LSVs) in THF (0.1 M Bu_4NPF_6) solution containing 1.0 M trifluoroacetic acid (TFA) in the absence (black) and presence of Au_{25} (red) and $PtAu_{24}$ (blue) clusters at a glassy carbon electrode (GCE). Compared to the blank current, the current for the proton reduction is significantly increased in the presence of Au_{25}. The current further increases in the presence of $PtAu_{24}$. The onset potential (E_{onset}) of catalytic current is observed at -1.10 V for Au_{25}, positively shifted by 150 mV compared to that of the blank GCE. In the presence of $PtAu_{24}$, the onset was found at -0.89 V, positively shifted by 360 mV. The thermodynamic reduction potential of proton is estimated to be -0.82 V in THF (1.0 M TFA) and thus the onset potential of -0.89 observed for $PtAu_{24}$ corresponds to an overpotential of 70 mV (refs 35,36), which is comparable to that of natural hydrogenase ($\sim$100 mV) enzymes[37].

The catalytic activity of $PtAu_{24}$ was further examined with increasing the concentration of TFA. As shown in Fig. 2c, the LSV clearly shows current peaks at -0.76 and -1.10 V corresponding to the first and second reduction of the $PtAu_{24}$ cluster. Whereas there is no significant change observed for the $[PtAu_{24}]^{0/-}$ peak, the $[PtAu_{24}]^{-/2-}$ peak current drastically increases with TFA, suggesting that HER is greatly enhanced at the potential where $[PtAu_{24}]^{2-}$ is formed. That the HER current increases at the potential of the $[PtAu_{24}]^{-/2-}$ couple strongly suggests that $PtAu_{24}$ acts as an electron transfer mediator for HER that shuttles electrons from GCE to proton in the solution[38,39]. Interestingly, the onset potential of the second

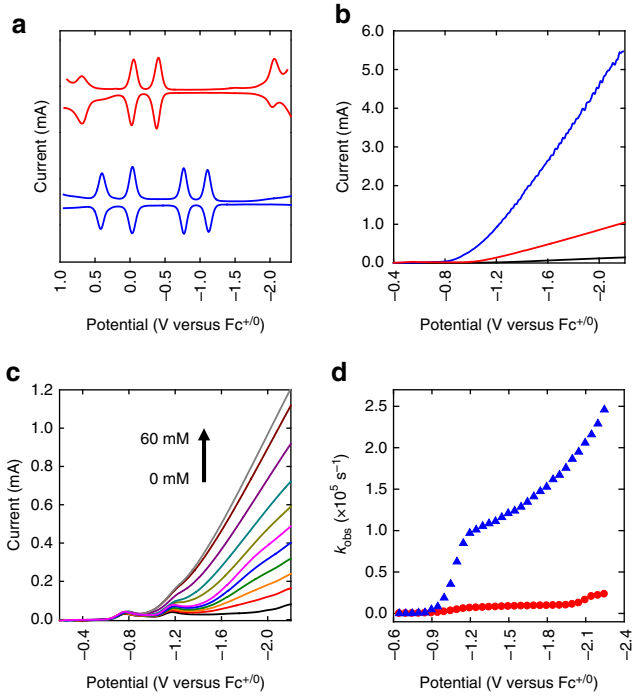

Figure 2 | Voltammograms and electrocatalytic activities of metal clusters. (**a**) SWVs of Au_{25} (red) and $PtAu_{24}$ (blue) in CH_2Cl_2 (0.1 M Bu_4NPF_6). (**b**) LSVs in THF (0.1 M Bu_4NPF_6) solution containing 1.0 M TFA in the absence (black) and presence of 1 mM Au_{25} (red) and 1 mM $PtAu_{24}$ (blue) at 50 mVs^{-1}. (**c**) LSVs of $PtAu_{24}$ (1 mM) in THF (0.1 M Bu_4NPF_6) at 50 mVs^{-1} in the presence of 0, 4, 8, 12, 17, 21, 27, 34, 45, 55 and 60 mM of TFA. (**d**) k_{obs}-potential plots for Au_{25} (red) and $PtAu_{24}$ (blue) in the presence of 1.0 M TFA. For the precise comparison, measured potentials were corrected using ferrocene ($Fc^{+/0}$) as an internal standard.

reduction of $PtAu_{24}$ matches well with the E_{onset} (-0.89 V) observed in Fig. 2b, suggesting that the HER catalytic activity is indeed dependent on the charge state of $PtAu_{24}$. When the catalytic activity of Au_{25} was examined with increasing concentration of TFA, the current increase at a more negative potential (-1.1 V) and the reduction current associated with HER was found to be much smaller (Supplementary Fig. 2). This result unambiguously shows that Pt doping significantly alters the redox potentials of the host cluster and thus drastically enhance its catalytic activity. In addition, the charge-state-dependent catalytic activity of $PtAu_{24}$ clusters indicates that they are like molecular catalysts that carry discrete charge for reaction, which sets these clusters apart from other metal nanoparticle systems.

At sufficiently high acid concentration relative to the catalyst, the following equation can be used to calculate pseudo-first-order rate constant, k_{obs}, for H_2 evolution that is catalysed by freely diffusing catalysts:[6,13,40]

$$\frac{I_c}{I_p} = \frac{2}{0.446}\sqrt{\frac{RTk_{obs}}{Fv}} \quad (1)$$

where I_c is the catalytic current, I_p is the peak current in the absence of acid (here taken from the wave of $[PtAu_{24}]^{0/-}$ or $[Au_{25}]^{0/-}$), 2 is the number of electrons involved in the catalytic reaction, R is the ideal gas constant, T is the temperature in Kelvin, F is Faraday's constant and v is the scan rate. As can be seen in Supplementary Fig. 3a, I_c increases with increasing acid concentration and levels off above 1.0 M TFA. At the acid concentration of 1.0 M, k_{obs} was then obtained by plotting I_c/I_p as a function of $v^{-1/2}$ as shown in Supplementary Fig. 3b. The k_{obs} value calculated from the slope of the fit line (Supplementary Fig. 3b) is 121,000 s^{-1} at -1.5 V ($\eta = 650$ mV). Under the same experimental condition, the k_{obs} value calculated in the presence of Au_{25} is only 8,000 s^{-1}. The rate constant observed for $PtAu_{24}$ is also significantly higher than those reported to date for highly active molecular electrocatalysts; compared to cobalt complexes (700 s^{-1} at $\eta = 890$ mV)[41] and copper complexes (11,000 s^{-1} at $\eta = 720$ mV)[13] in comparable conditions, it is ca. 170- and 11-fold higher, respectively. To the best of our knowledge, the highest k_{obs} value (106,000 s^{-1}) thus far reported was observed at $\eta = 650$ mV for a nickel complex that catalyses H_2 formation with pendant amines that act as proton relays[6]. The k_{obs} value obtained for $PtAu_{24}$ is also higher than that.

To understand the origin of the extraordinary catalytic activity observed for $PtAu_{24}$, we compared k_{obs} as a function of potential. As can be seen in Fig. 2d, the k_{obs} value found at -0.89 V is 1,300 s^{-1} and sharply increases to 62,000 s^{-1} at -1.1 V, followed by a gradual increase to 186,000 s^{-1} at -2.0 V. Interestingly, the potential where the drastic increase occurs matches well with the second reduction wave $[PtAu_{24}]^{-/2-}$. By contrast, the k_{obs} value calculated for Au_{25} is found to be relatively small ($<16{,}000\ s^{-1}$) until -2.1 V, where $[Au_{25}]^-$ is reduced to $[Au_{25}]^{2-}$.

Mechanisms of HER. The mechanism study shown in Fig. 3 clearly exhibits the charge-state-dependent catalytic activity of $PtAu_{24}$. That is, the catalytic currents observed at potentials negative to the $[PtAu_{24}]^{-/2-}$ wave (that is, -1.3, -1.8 and -2.2 V) all exhibit linear correlation with $[PtAu_{24}]$ and $[TFA]^{1/2}$, respectively, which is consistent with the heterolytic HER mechanism (equation (3))[42,43]. On the other hand, at -1.0 V where $PtAu_{24}$ is predominantly present in the form of $[PtAu_{24}]^-$, the currents exhibit linear correlation with [TFA] and $[PtAu_{24}]^{3/2}$, respectively, as shown in Fig. 3 insets, indicating the homolytic HER mechanism (equation (4))[42].

$$[PtAu_{24}]^0 \xrightarrow{2e^-} [PtAu_{24}]^{2-} \xrightarrow{H^+} [H{-}PtAu_{24}]^- \quad (2)$$

Heterolytic pathway:

$$[H{-}PtAu_{24}]^- + H^+ \rightarrow [PtAu_{24}]^0 + H_2 \quad (3)$$

Homolytic pathway:

$$[H{-}PtAu_{24}]^0 + [H{-}PtAu_{24}]^0 \rightarrow 2\,[PtAu_{24}]^0 + H_2 \quad (4)$$

This result is very reasonable considering the charge state of $PtAu_{24}$. $[PtAu_{24}]^{2-}$ reacts with proton to form $[H\text{-}PtAu_{24}]^-$ intermediate that is negatively charged and thus preferably react with proton to evolve H_2. On the other hand, at -1.0 V $[PtAu_{24}]^-$ reacts with proton to form $[H\text{-}PtAu_{24}]^0$ intermediate that favours homolytic HER pathway. Similar charge-state dependence is observed for Au_{25}. As shown in Supplementary Fig. 4, the catalytic currents exhibit linear correlation with [TFA] and $[Au_{25}]^{3/2}$, respectively, indicating homolytic pathway, at -1.0, -1.3 and -1.8 V, where Au_{25} clusters are present in the form of $[Au_{25}]^-$. When the cluster is reduced to $[Au_{25}]^{2-}$ at -2.2 V, the currents exhibit linear correlation with $[TFA]^{1/2}$ and $[Au_{25}]$, respectively, as shown in the insets of Supplementary Fig. 4, indicating the heterolytic HER pathway. The charge-state-dependent catalytic activity has been observed for electrocatalysis using Co complexes where $[Co(II)H]^-$ favours heterolytic HER pathway, while homolytic pathway is favoured by $[Co(III)H]^0$ intermediate[44]. The charge-state-dependent catalytic activity of $PtAu_{24}$ observed in this work clearly display the characteristic of molecular catalysts.

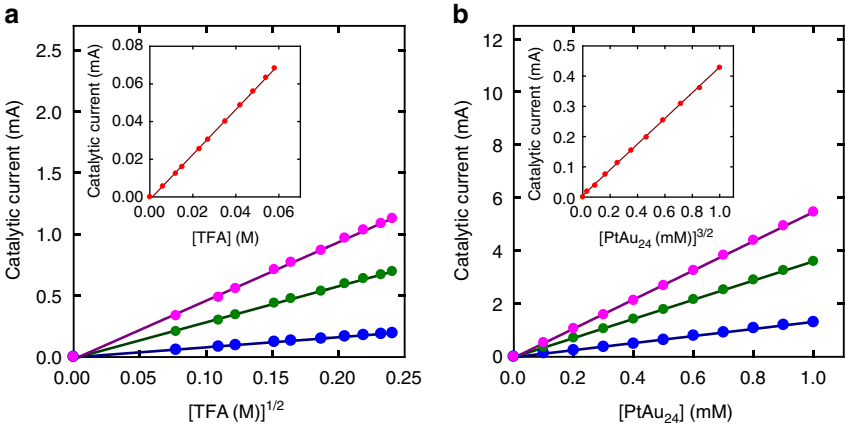

Figure 3 | Charge-state-dependent electrochemical HER mechanisms catalysed by $PtAu_{24}$. Dependence of the catalytic current, I_c, (**a**) on the concentration of TFA in the presence of $PtAu_{24}$ (1 mM) and (**b**) on the concentration of $PtAu_{24}$ in TFA (1.0 M) solution at −1.3 (blue), −1.8 (green) and −2.2 V (purple). Insets show plots for dependence of the I_c on the concentration of (**a**) TFA and (**b**) $PtAu_{24}$ at −1.0 V. The data are fitted by first-order linear functions (solid lines).

The charge state is not the only factor affecting the HER activity of the clusters. Comparing $[PtAu_{24}]^{2-}$ with $[Au_{25}]^{2-}$, the k_{obs} value calculated for $[PtAu_{24}]^{2-}$ is 229,000 s^{-1}, more than 10-fold higher than that of $[Au_{25}]^{2-}$ (22,000 s^{-1}) at −2.2 V at which both clusters are present as a dianionic form. The vastly different catalytic activity can be understood by considering the reduction potential match between the catalyst and the substrate (proton). That is, when the reduction potential of catalyst matches closely with the thermodynamic potential of proton, the catalyst can act as an effective electron transfer mediator and enhance its activity dramatically[41,45,46]. In this work, the reduction potential of catalyst can be precisely tuned to match with the potential of HER by Pt doping, enabling judiciously optimized electrocatalysis.

To gain further insight into the origin of the extraordinary catalytic activity of $PtAu_{24}$, we have compared the hydrogen adsorption and the HER energetics calculated using density functional theory (DFT) for each cluster. We modelled the HER process by using protons solvated by two THF molecules, which are then adsorbed on the cluster surface; the whole system is further solvated by an implicit solvation model. Figure 4 shows that the energy change of the Volmer step (step 1) calculated for $[PtAu_{24}]^{2-}$ is rather thermodynamically neutral (−0.059 eV), whereas that for $[Au_{25}]^{-}$ is 0.539 eV. This result clearly suggests the initial hydrogen binding is energetically favourable on $[PtAu_{24}]^{2-}$, but is endothermic on $[Au_{25}]^{-}$, explaining the high HER activity observed for $[PtAu_{24}]^{2-}$. However, the second H adsorption on $[PtAu_{24}]^{2-}$ and $[Au_{25}]^{-}$ is found to be both endothermic; 0.369 and 1.21 eV for $[H\text{-}PtAu_{24}]^{-}$ (step 2a in Fig. 4) and $[H\text{-}Au_{25}]^{0}$, respectively. Thus, the DFT calculations predict that hydrogen evolution occurs on $PtAu_{24}$ via the coupling of the adsorbed hydrogen with another proton from the solution (that is, heterolytic or Heyrovsky pathway) with an energy change of −0.155 eV (step 2b in Fig. 4). By contrast, the most thermodynamically favourable H_2 generation occurs on Au_{25} via the homolytic pathway (Supplementary Fig. 5). These calculation results are indeed in consistent with the experimentally found HER mechanisms for $[PtAu_{24}]^{2-}$ and $[Au_{25}]^{-}$. The idea of thermoneutral catalysts for HER regarding hydrogen binding has been demonstrated experimentally for pure metals, alloys and layered solid catalysts[16–18,47]. Recently, it has been pointed out that this concept can be applied to molecular complexes, although it is significantly difficult to find the thermoneutral complexes because of their inherently complex chemical environment[17,35,48]. In this work, we have demonstrated that the redox potentials and binding affinity can be fine-tuned by simple doping of a Pt atom into gold catalysts, opening a new avenue to the fine-tuning of the catalytic properties.

Figure 4 also shows that the hydrogen preferably binds on the hollow site of the surface of the $PtAu_{12}$ core. It is interesting to note that the bond distance between the central Pt and the adsorbed H is found to be 1.788 Å, significantly shorter than the distance between the surface Au and the adsorbed H (2.031 Å), indicating that the adsorbed H atom forms H-Pt chemical bond with the central Pt. In the DFT calculations, we initially placed the H atom on the intact cluster surface away from the Au atoms; during geometry optimization, we found that the H atom spontaneously moves into the subsurface to interact directly with the central Pt atom while breaking some surface Au-Au bonds. This result suggests that the H-Pt bond formation is a downhill process with no transition state. The H-Pt bond is also manifested in the local electronic density of states (Supplementary Fig. 6) that shows the hybridization between Pt 5*d* states and the H 1*s* state. The stronger H–Pt interaction than the H–Au interaction is a key factor contributing to the favourable HER energetics (Fig. 4) on $[PtAu_{24}]^{2-}$ than on $[Au_{25}]^{-}$.

Electrocatalytic H_2 production. To verify the catalytic production of H_2, we carried out controlled potential electrolysis (CPE) with $PtAu_{24}$ in THF containing 1.0 M TFA in an H-type cell. Figure 5a shows plots of the average current density and the amount of H_2 detected by gas chromatography analysis at each overpotential. The clusters display symptoms of decomposition after prolonged CPE experiments and thus the electrolysis was conducted for 15 min. As can be seen in the figure, production of H_2 is first detected at an overpotential of 0.2 V and increases with increasing overpotential. Comparison of the amount of H_2 produced with the charge consumed indicates that the current efficiency for H_2 production is > 97% when the overpotential is 0.4 V or higher. After subtracting the H_2 production from the blank solution, the TOF at $\eta = 0.6$ V is found to be 4.8 mol H_2 (mol cat)$^{-1}$ s^{-1}. To the best of our knowledge, this value is considerably higher than any other molecular catalysts reported for HER in similar conditions[6–9,12,13]. The highest TOF value reported thus far is 4.1 mol H_2 (mol cat)$^{-1}$ s^{-1} obtained for a

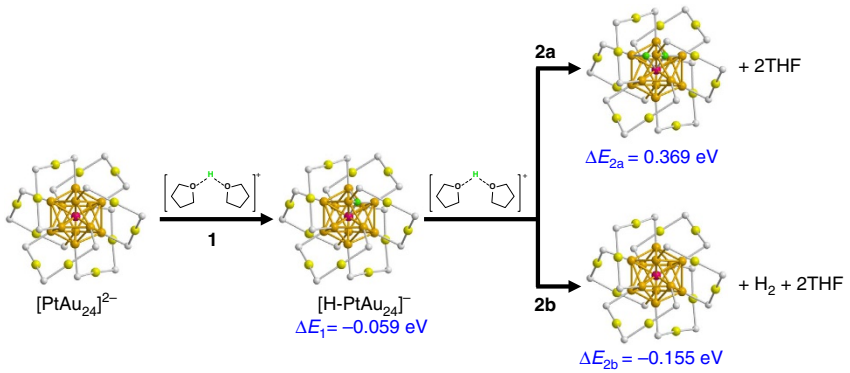

Figure 4 | Calculated reaction energies for H_2 evolution on $PtAu_{24}$. In step 1, a solvated proton is transferred from THF molecules to $[PtAu_{24}]^{2-}$ to form $[H\text{-}PtAu_{24}]^{-}$; in step 2a, a second solvated proton is transferred from THF molecules to $[H\text{-}PtAu_{24}]^{-}$ to form $[2H\text{-}PtAu_{24}]$; in step 2b, a second solvated proton reacts with H in $[H\text{-}PtAu_{24}]^{-}$ to form H_2. The calculations are at the DFT-TPSS level; besides the two explicit solvent molecules, an implicit solvent model is also included for the whole system (see 'Methods' section). Colour code for the cluster structure: golden, Au atoms of the core; olive, Au atoms of the shell; purple, Pt atom; green, adsorbed H from the liquid medium; grey, S (the rest of ligand is omitted for clarity).

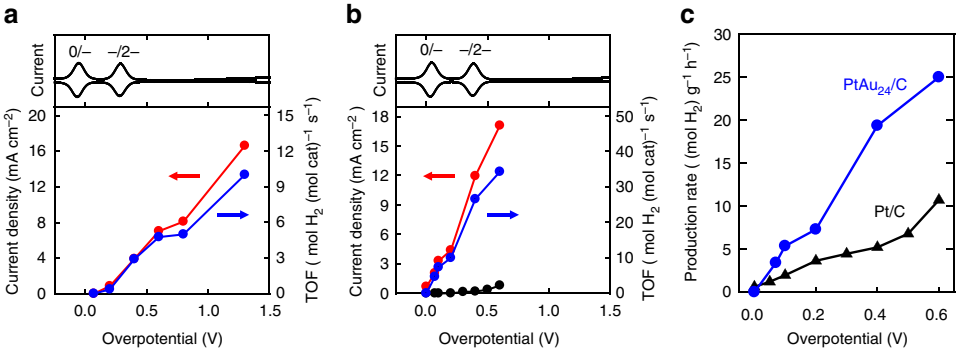

Figure 5 | CPE data for $PtAu_{24}$ in homogeneous and heterogeneous conditions. (**a**) Average current densities (red circles) and TOFs (blue circles) obtained at various overpotentials after 15 min homogeneous CPE in THF (0.5 M Bu_4NPF_6) containing 1.0 TFA with a glassy carbon plate (1 cm^2) in the presence of $PtAu_{24}$ (2.5 μM). (**b**) Average current densities (red circles) and TOFs (blue circles) obtained at various overpotentials after 60 min heterogeneous CPE in 1.0 M Brinton–Robinson buffer solution (pH 3) on a $PtAu_{24}$/C/GDL electrode (1 cm^2). Average current densities obtained on a blank C/GDL (black circles) are shown for comparison. SWVs of $PtAu_{24}$ shown in the upper part of the graphs show the charge state of $PtAu_{24}$ at each overpotential. (**c**) H_2 production rates per mass of metals in the catalyst ((mol H_2) $g^{-1} h^{-1}$) at various overpotentials on a $PtAu_{24}$/C/GDL (blue circles) and a Pt/C/GDL (black triangles) electrodes (1 cm^2).

copper complex at a higher overpotential of 0.75 V (ref. 13). The nickel complex exhibiting a k_{obs} value of 106,000 s^{-1} shows a TOF of 0.24 mol H_2 (mol cat)$^{-1}$ s^{-1} at $\eta = 0.92$ V (ref. 6).

While $PtAu_{24}$ exhibits high catalytic activity for H_2 production with moderate overpotential requirements in a non-aqueous solvent, it would be more practical if it can be immobilized on electrode materials that can fully operate in aqueous media. There are a number of immobilization strategies available for gold nanoparticles via their surface functionalization[39,49,50]. In this work, $PtAu_{24}$ cluster solution mixed with a carbon black (C) and Nafion was dropcast on a gas diffusion layer (GDL) electrode ($PtAu_{24}$/C/GDL). We found that the clusters immobilized on the carbon black with the Nafion binder exhibit higher stability during electrolysis. Figure 5b shows plots of the average current density and the amount of H_2 detected after 60 min CPE at each overpotential in 1.0 M Brinton–Robinson buffer solution (pH 3). As can be seen in the figure, H_2 generation was achieved near the thermodynamic potential ($\eta = 70$ mV), which also matches very well with the E_{onset} found in Fig. 2b. The charge passed and H_2 generation increased rapidly with increasing overpotential and the current efficiency for HER went up to nearly 100% when the overpotential is 100 mV or higher. At $\eta = 400$ mV, the average current density increases above 12 mA cm^{-2}. Having immobilized such well-defined clusters on the electrode, we were able to calculate the TOF from the CPE experiments. As can be seen in Fig. 5b, the TOF values obtained from the heterogeneous catalysis are remarkably high; 34 mol H_2 (mol cat)$^{-1}$ s^{-1} at $\eta = 0.6$ V in aqueous media after subtracting the contribution from the blank C/GDL electrode. This value is again much higher than those obtained in comparable conditions. For comparison, a TOF of 2.2 mol H_2 (mol cat)$^{-1}$ s^{-1} was obtained at $\eta = 0.59$ V in acetate buffer (pH 4.5) for a cobalt catalyst immobilized on carbon nanotubes[14].

Although it is not straightforward to directly compare the TOF values obtained from the homogeneous (Fig. 5a) and heterogeneous (Fig. 5b) catalysis, the enhanced TOF obtained in the latter in aqueous media is highly encouraging and may reflect the fact that all clusters on the electrode are available for catalysis. The high catalytic activity observed for the $PtAu_{24}$/C/GDL electrode has prompted us to compare its activity with the benchmarking Pt/C (commercial 20 wt% Pt on Vulcan carbon black) dropcast on a GDL electrode (1 cm^2). Since TOF could not be determined for the Pt/C, we have compared the H_2 production rate per mass of metals (that is, Au + Pt) in the catalyst composites (mol H_2 $g^{-1} h^{-1}$). As can be seen in Fig. 5c, both $PtAu_{24}$/C/GDL and Pt/C/GDL electrodes start to produce H_2

near the thermodynamic potential, but the H_2 production rate determined for the $PtAu_{24}$/C/GDL is much higher than that for the Pt/C/GDL. For instance, the H_2 production rate determined for the $PtAu_{24}$/C/GDL is 25 mol $H_2\,g^{-1}\,h^{-1}$, which is more than two times higher than that for the Pt/C/GDL catalyst (11 mol $H_2\,g^{-1}\,h^{-1}$) at the same overpotential of 0.6 V.

Discussion

Here we show that the electronic structure and the catalytic activity of a cluster catalyst can be fine controlled by doping a Pt atom into a stable gold cluster. The bimetallic cluster is molecule-like and exhibits excellent catalytic activity for H_2 production; significantly higher than any other molecular catalysts reported thus far, to the best of our knowledge, and even higher than the benchmarking platinum catalyst. Mechanistic investigations have revealed that hydrogen binding step on the bimetallic cluster is thermodynamically neutral and the central Pt atom forms Pt-H chemical bond, pointing to a key role of the dopant. The molecule-like bimetallic cluster operates efficiently in both homogeneous and heterogeneous conditions, representing a special type of electrocatalyst. The molecule-like bimetallic cluster may thus provide a platform for the discovery of finely tuned catalysts, which could have broad implications for catalysis beyond H_2 production.

Methods

Electrochemical methods. SWV and LSV were conducted with an electrochemical workstation (model 660B; CH Instruments) in CH_2Cl_2 (SWV) or THF (LSV) containing 0.1 M Bu_4NPF_6 as a supporting electrolyte that was degassed and blanketed with a high-purity Ar gas. A GCE (3 mm diameter) was used as a working electrode, a Pt wire as the counter electrode and $Ag/AgNO_3$ (0.1 M $AgNO_3$ in CH_3CN) as the reference electrode for the LSV experiments. SWV was carried out with a Pt disk (0.4 mm diameter) working electrode at 100 mV s^{-1} with a pulse height and a width of 20 mV and 20 ms, respectively. Ferrocene ($Fc^{+/0}$) was added as an internal reference for $Ag/AgNO_3$.

Controlled potential electrolysis. CPE experiments in homogeneous condition were conducted in a 5 ml cell containing 2.5 μM cluster and 1.0 M TFA dissolved in 2.0 ml THF (0.5 M Bu_4NPF_6) that was degassed and blanketed with Ar gas. Electrolysis was conducted for 15 min under vigorous stirring with an electrochemical workstation (model 660B; CH Instruments) equipped with three electrodes consisting of glassy carbon plate working electrode (area = 1 cm^2), a GDL (model N1S1007; CeTech Co., Taiwan) counter electrode (1 cm^2) and a $Ag/AgNO_3$ reference electrode. CPE experiments in heterogeneous condition were carried out for 60 min under vigorous stirring with a ZIVE MP1 potentiostat (WonATech, Korea) in an H-type cell that was equipped with a composite working electrode and a Ag/AgCl (3 M NaCl) reference electrode in one compartment and a platinum plate (1.68 cm^2) counter electrode in the other compartment. The working electrode was separated from the counter electrode by a proton exchange membrane (Nafion 117; Sigma-Aldrich). Both compartments were filled with 60 ml of 1.0 M Brinton–Robinson buffer (pH 3.0) that was degassed and blanketed with Ar gas. The composite working electrode was fabricated by spreading a catalyst ink prepared by mixing 16 μg of the cluster catalyst, 200 μg of carbon black (Vulcan XC-72) and 1.5 μl of Nafion solution (5 wt%; Sigma-Aldrich) in 50 μl of THF on a GDL (N1S1007; CeTech Co.) electrode (1 cm^2). For comparison, CPE experiments were conducted under the same condition using a commercial Pt/C (20 wt% platinum on Vulcan carbon black; Sigma-Aldrich) catalyst that was mixed with Nafion and dropcast on a GDL electrode (1 cm^2). The average size of Pt particle was 3.5 ± 0.5 nm. The amount of H_2 evolved was quantified from an analysis of the headspace using an Agilent 7890B gas chromatography equipped with a thermal conductivity detector.

Computational methods. DFT calculations of the HER on $Au_{25}(SCH_3)_{18}$ and $PtAu_{24}(SCH_3)_{18}$ clusters were performed with the quantum chemistry program Turbomole V6.5. The def2-SV(P) basis sets were used for C, S and H, while effective core potentials which include scalar relativistic corrections and 19 (18) valence electrons were used for Au (Pt). Geometry optimization was done with the TPSS (Tao, Perdew, Staroverov and Scuseria) functional. In our calculations, solvent effects were treated implicitly by making use of the conductor-like screening model (COSMO) as implemented in Turbomole.

Data availability. The authors declare that all the other data supporting the findings of this study are available within the article and its Supplementary Information Files or from the corresponding author on reasonable request.

References

1. Holladay, J. D., Hu, J., King, D. L. & Wang, Y. An overview of hydrogen production technologies. *Catal. Today* **139,** 244–260 (2009).
2. Zheng, Y., Jiao, Y., Jaroniec, M. & Qiao, S. Z. Advancing the electrochemistry of the hydrogen-evolution reaction through combining experiment and theory. *Angew. Chem. Int. Ed.* **54,** 52–65 (2015).
3. Bullock, R. M., Appel, A. M. & Helm, M. L. Production of hydrogen by electrocatalysis: making the H-H bond by combining protons and hydrides. *Chem. Commun.* **50,** 3125–3143 (2014).
4. Thoi, V. S., Sun, Y., Long, J. R. & Chang, C. J. Complexes of earth-abundant metals for catalytic electrochemical hydrogen generation under aqueous conditions. *Chem. Soc. Rev.* **42,** 2388–2400 (2013).
5. Pershad, H. R. *et al.* Catalytic electron transport in chromatium vinosum [NiFe]-hydrogenase: application of voltammetry in detecting redox-active centers and establishing that hydrogen oxidation is very fast even at potentials close to the reversible H^+/H_2 value. *Biochemistry* **38,** 8992–8999 (1999).
6. Helm, M. L., Stewart, M. P., Bullock, R. M., DuBois, M. R. & DuBois, D. L. A synthetic nickel electrocatalyst with a turnover frequency above 100,000 s^{-1} for H_2 production. *Science* **333,** 863–866 (2011).
7. Hoffert, W. A., Roberts, J. A. S., Bullock, R. M. & Helm, M. L. Production of H_2 at fast rates using a nickel electrocatalyst in water-acetonitrile. *Chem. Commun.* **49,** 7767–7769 (2013).
8. McCrory, C. C. L., Uyeda, C. & Peters, J. C. Electrocatalytic hydrogen evolution in acidic water with molecular cobalt tetraazamacrocycles. *J. Am. Chem. Soc.* **134,** 3164–3170 (2012).
9. Chen, L. *et al.* A super-efficient cobalt catalyst for electrochemical hydrogen production from neutral water with 80 mV overpotential. *Energy Environ. Sci.* **7,** 329–334 (2014).
10. Tard, C. *et al.* Synthesis of the H-cluster framework of iron-only hydrogenase. *Nature* **433,** 610–613 (2005).
11. Symes, M. D. & Cronin, L. Decoupling hydrogen and oxygen evolution during electrolytic water splitting using an electron-coupled-proton buffer. *Nat. Chem.* **5,** 403–409 (2013).
12. Karunadasa, H. I., Chang, C. J. & Long, J. R. A molecular molybdenum-oxo catalyst for generating hydrogen from water. *Nature* **464,** 1329–1333 (2010).
13. Zhang, P., Wang, M., Yang, Y., Yao, T. & Sun, L. A molecular copper catalyst for electrochemical water reduction with a large hydrogen-generation rate constant in aqueous solution. *Angew. Chem. Int. Ed.* **53,** 13803–13807 (2014).
14. Andreiadis, E. S. *et al.* Molecular engineering of a cobalt-based electrocatalytic nanomaterial for H_2 evolution under fully aqueous conditions. *Nat. Chem.* **5,** 48–53 (2013).
15. Goff, A. L. *et al.* From hydrogenases to noble metal-free catalytic nanomaterials for H_2 production and uptake. *Science* **326,** 1384–1387 (2009).
16. Zeng, M. & Li, Y. Recent advances in heterogeneous electrocatalysts for the hydrogen evolution reaction. *J. Mater. Chem. A* **3,** 14942–14962 (2015).
17. Wodrich, M. D., Busch, M. & Corminboeuf, C. Accessing and predicting the kinetic profiles of homogeneous catalysts from volcano plots. *Chem. Sci.* **7,** 5723–5735 (2016).
18. Greeley, J., Jaramillo, T. F., Bonde, J., Chorkendorff, I. & Nørskov, J. K. Computational high-throughput screening of electrocatalytic materials for hydrogen evolution. *Nat. Mater.* **5,** 909–913 (2006).
19. Murray, R. W. Nanoelectrochemistry: metal nanoparticles, nanoelectrodes, and nanopores. *Chem. Rev.* **108,** 2688–2720 (2008).
20. Li, G. & Jin, R. Atomically precise gold nanoclusters as new model catalysts. *Acc. Chem. Res.* **46,** 1749–1758 (2013).
21. Jin, R. Atomically precise metal nanoclusters: stable sizes and optical properties. *Nanoscale* **7,** 1549–1565 (2015).
22. Maity, P., Xie, S., Yamauchi, M. & Tsukuda, T. Stabilized gold clusters: from isolation toward controlled synthesis. *Nanoscale* **4,** 4027–4037 (2012).
23. Tyo, E. C. & Vajda, S. Catalysis by clusters with precise numbers of atoms. *Nat. Nanotechnol.* **10,** 577–588 (2015).
24. Gracia-Espino, E., Jia, X. & Wågberg, T. Improved oxygen reduction performance of Pt-Ni nanoparticles by adhesion on nitrogen-doped graphene. *J. Phys. Chem. C* **118,** 2804–2811 (2014).
25. Tofanelli, M. A. & Ackerson, C. J. Superatom electron configuration predicts thermal stability of $Au_{25}(SR)_{18}$ nanoclusters. *J. Am. Chem. Soc.* **134,** 16937–16940 (2012).
26. Walter, M. *et al.* A unified view of ligand-protected gold clusters as superatom complexes. *Proc. Natl Acad. Sci. USA* **105,** 9157–9162 (2008).
27. Harkness, K. M. *et al.* $Ag_{44}(SR)_{30}^{4-}$: a silver-thiolate superatom complex. *Nanoscale* **4,** 4269–4274 (2012).

28. Negishi, Y., Iwai, T. & Ide, M. Continuous modulation of electronic structure of stable thiolate-protected Au_{25} cluster by Ag doping. *Chem. Commun.* **46,** 4713–4715 (2010).
29. Negishi, Y., Munakata, K., Ohgake, W. & Nobusada, K. Effect of copper doping on electronic structure, geometric structure, and stability of thiolate-protected Au_{25} nanoclusters. *J. Phys. Chem. Lett.* **3,** 2209–2214 (2012).
30. Qian, H. *et al.* Monoplatinum doping of gold nanoclusters and catalytic application. *J. Am. Chem. Soc.* **134,** 16159–16162 (2012).
31. Niihori, Y., Kurashige, W., Matsuzaki, M. & Negishi, Y. Remarkable enhancement in ligand-exchange reactivity of thiolate-protected Au_{25} nanoclusters by single Pd atom doping. *Nanoscale* **5,** 508–512 (2013).
32. Miller, S. A., Fields-Zinna, C. A., Murray, R. W. & Moran, A. M. Nonlinear optical signatures of core and ligand electronic states in $Au_{24}PdL_{18}$. *J. Phys. Chem. Lett.* **1,** 1383–1387 (2010).
33. Tian, S. *et al.* Structures and magnetism of mono-palladium and mono-platinum doped $Au_{25}(PET)_{18}$ nanoclusters. *Chem. Commun.* **52,** 9873–9876 (2016).
34. Kwak, K., Tang, Q., Kim, M., Jiang, D.-e. & Lee, D. Interconversion between superatomic 6-electron and 8-electron configurations of $M@Au_{24}(SR)_{18}$ clusters (M = Pd, Pt). *J. Am. Chem. Soc.* **137,** 10833–10840 (2015).
35. Marinescu, S. C., Winkler, J. R. & Gray, H. B. Molecular mechanisms of cobalt-catalyzed hydrogen evolution. *Proc. Natl Acad. Sci. USA* **109,** 15127–15131 (2012).
36. Felton, G. A. N., Glass, R. S., Lichtenberger, D. L. & Evans, D. H. Iron-only hydrogenase mimics. Thermodynamic aspects of the use of electrochemistry to evaluate catalytic efficiency for hydrogen generation. *Inorg. Chem.* **45,** 9181–9184 (2006).
37. Lubitz, W., Ogata, H., Rüdiger, O. & Reijerse, E. Hydrogenases. *Chem. Rev.* **114,** 4081–4148 (2014).
38. Armstrong, F. A. & Wilson, G. S. Recent developments in faradaic bioelectrochemistry. *Electrochim. Acta* **45,** 2623–2645 (2000).
39. Kumar, S. S., Kwak, K. & Lee, D. Electrochemical sensing using quantum-sized gold nanoparticles. *Anal. Chem.* **83,** 3244–3247 (2011).
40. Pool, D. H. & DuBois, D. L. $[Ni(P^{Ph}{}_2N^{Ar}{}_2)_2(NCMe)][BF_4]_2$ as an electrocatalyst for H_2 production: $P^{Ph}{}_2N^{Ar}{}_2$ = 1,5-(di(4-(thiophene-3-yl)phenyl)-3,7-diphenyl-1,5-diaza-3,7-diphosphacyclooctane. *J. Organomet. Chem.* **694,** 2858–2865 (2009).
41. Hu, X., Brunschwig, B. S. & Peters, J. C. Electrocatalytic hydrogen evolution at low overpotentials by cobalt macrocyclic glyoxime and tetraimine complexes. *J. Am. Chem. Soc.* **129,** 8988–8998 (2007).
42. Rountree, E. S., McCarthy, B. D., Eisenhart, T. T. & Dempsey, J. L. Evaluation of homogeneous electrocatalysts by cyclic voltammetry. *Inorg. Chem.* **53,** 9983–10002 (2014).
43. Valdez, C. N., Dempsey, J. L., Brunschwig, B. S., Winkler, J. R. & Gray, H. B. Catalytic hydrogen evolution from a covalently linked dicobaloxime. *Proc. Natl Acad. Sci. USA* **109,** 15589–15593 (2012).
44. Solis, B. H. & Hammes-Schiffer, S. Theoretical analysis of mechanistic pathways for hydrogen evolution catalyzed by cobaloximes. *Inorg. Chem.* **50,** 11252–11262 (2011).
45. Rees, D. C. Electrostatic influence on energetics of electron transfer reactions. *Proc. Natl Acad. Sci. USA* **82,** 3082–3085 (1985).
46. Collman, J. P., Ha, Y., Wagenknecht, P. S., Lopez, M. A. & Guilard, R. Cofacial bisorganometallic diporphyrins: synthetic control in proton reduction catalysis. *J. Am. Chem. Soc.* **115,** 9080–9088 (1993).
47. Tymoczko, J., Calle-Vallejo, F., Schuhmann, W. & Bandarenka, A. S. Making the hydrogen evolution reaction in polymer electrolyte membrane electrolysers even faster. *Nat. Commun.* **7,** 10990 (2016).
48. Koper, M. T. M. & Bouwman, E. Electrochemical hydrogen production: bridging homogeneous and heterogeneous catalysis. *Angew. Chem. Int. Ed.* **49,** 3723–3725 (2010).
49. Vargo, M. L. *et al.* Distance dependence of electron transfer kinetics for azurin protein adsorbed to monolayer protected nanoparticle film assemblies. *Langmuir* **26,** 560–569 (2010).
50. Kwak, K., Kumar, S. S., Pyo, K. & Lee, D. Ionic liquid of a gold nanocluster: a versatile matrix for electrochemical biosensors. *ACS Nano* **8,** 671–679 (2014).

Acknowledgements

This work was supported by the Korea CCS R&D Center (KCRC) Grant (NRF-2014M1A8A1074219). Q.T. was supported by the University of California, Riverside; D.-e.J. was supported by the U.S. Department of Energy, Office of Science, Office of Basic Energy Sciences, Chemical Sciences, Geosciences, and Biosciences Division.

Author contributions

K.K., W.C. and D.L. planned the research. K.K., W.C., M.K. and Y.L. performed the experiments. Q.T. and D.-e.J. carried out the DFT calculations. K.K., D.-e.J. and D.L. prepared the manuscript.

Additional information

Supplementary Information accompanies this paper at http://www.nature.com/naturecommunications

Competing financial interests: The authors declare no competing financial interests.

Reprints and permission information is available online at http://npg.nature.com/reprintsandpermissions/

How to cite this article: Kwak, K. *et al.* A molecule-like $PtAu_{24}(SC_6H_{13})_{18}$ nanocluster as an electrocatalyst for hydrogen production. *Nat. Commun.* **8,** 14723 doi: 10.1038/ncomms14723 (2017).

Publisher's note: Springer Nature remains neutral with regard to jurisdictional claims in published maps and institutional affiliations.